



Synchronous etching-epitaxial growth fabrication of facet-coupling NaTaO₃/Ta₂O₅ heterostructured nanofibers for enhanced photocatalytic hydrogen production

Leilei Xu, Xiaoli Sun, Hao Tu, Qian Jia, Haotian Gong, Jianguo Guan*

State Key Laboratory of Advanced Technology for Materials Synthesis and Processing, Wuhan University of Technology, Wuhan 430070, PR China

ARTICLE INFO

Article history:

Received 30 September 2015

Received in revised form

20 November 2015

Accepted 25 November 2015

Available online 28 November 2015

Keywords:

Tantalum oxide

Heterostructure

Facet-coupling

Synchronous etching-epitaxial growth

Photocatalytic hydrogen production

ABSTRACT

In this paper, we have developed a synchronous etching-epitaxial growth approach for the fabrication of facet-coupling NaTaO₃/Ta₂O₅ heterostructured nanofibers, where the NaTaO₃ nanocubes in-situ grow epitaxially along [121] on the crystal plane (110) of electrospun Ta₂O₅ nanofibers. In this protocol, elaborately adjusting the etching reaction kinetics of Ta₂O₅ can effectively regulate the heterogeneous nucleation and crystal growth rate of NaTaO₃, leading to form facet-coupling heterojunctions. Owing to facet-coupling heterojunction characters, the as-obtained NaTaO₃/Ta₂O₅ heterostructures show an improved light absorption and charge separation because of their reduced interfacial defects and the minimum charge transfer resistance. As a result, they even in the absence of any cocatalysts can exhibit a photocatalytic activity for hydrogen production as high as 1579 μmol h⁻¹ g⁻¹, far more than that of the corresponding Ta₂O₅, NaTaO₃ or the conventional heterostructured counterparts. The synchronous etching-epitaxial growth strategy developed here can be extended to the fabrication of other well-defined heterojunctions, especially of those whose precursors have a rapid hydrolysis rate. The as-obtained well-defined heterojunctions are promising for the effective utilization of solar energy by improving the separation and transfer efficiency of photogenerated charges.

© 2015 Elsevier B.V. All rights reserved.

1. Introduction

Semiconductor nanoheterostructures may define diverse functionalities arising from the interfacial interactions at nanoscale [1–3], and provide a unique means to promote the separation and transfer of photogenerated charge carriers [4–9]. Therefore, they have been recognized as an efficient strategy to increase light harvesting without worsening the separation of photogenerated charges and have promising applications in such active fields related to the solar energy utilization as photocatalysis and solar cells.

Tantalum-based materials, as a class of the most promising functional semiconductors, possess a more negative conduction band (CB) than most of the well-known photocatalytic materials, such as TiO₂, ZnS, and so on. Thus, they have attracted much attention to the overall water splitting for hydrogen production [10–14]. However, due to their rapid recombination of photogenerated charge carriers, they usually suffer from low photocatalytic hydrogen production efficiencies. Since the potential gradients between nanostructures

can offer the transfer driving force and thus dominate the transportation direction and distance of photogenerated charge carriers, constructing tantalum-based heterostructures, such as CdS/Ta₂O₅ [15], In₂O₃/Ta₂O₅ [16], Bi₂O₃/Bi-NaTaO₃ [17], NiO/NaTaO₃ [18], not only can significantly enhance the photogenerated charge separation, but also to some extent extend the light absorption range. However, due to the rapid hydrolysis rates of most tantalum-based precursors in aqueous solution and the high crystalline temperature, all the heterostructures reported so far usually exhibit the irregular morphologies, e.g., bulk or nanoparticle aggregates. Particularly, there often appear some unexpected defects at the interfaces. In this case, the enhancement of photocatalytic activity is greatly restricted for these heterostructures. Therefore, developing an efficient approach to fabricate tantalum-based heterostructures with well-defined interfaces is critical to further enhance the photocatalytic activity for hydrogen production of the tantalum-based heterostructures.

Recently, our group has successfully fabricated the hierarchical structure of Ta₂O₅ single crystalline rods via hydrolyzing H₂TaF₇ when it slowly forms by etching Ta powders with HF and H₂O₂ under hydrothermal conditions [19]. In this approach, the nucleation and growth rates of Ta₂O₅ are finely controlled by the etching kinetics of Ta powders, which drives the formation of well-defined

* Corresponding author. Fax: +86 27 87879468.

E-mail address: guanjq@whut.edu.cn (J. Guan).

structure of Ta₂O₅ with a higher crystallinity. As a result, the hierarchical structure of Ta₂O₅ single crystalline rods exhibits a greater photocatalytic activity. In view of this, we have developed a synchronous etching-growth approach for the fabrication of facet-coupling heterostructured NaTaO₃/Ta₂O₅ porous nanofibers with a good photocatalytic hydrogen production activity. In our fabrication strategy, the reaction kinetics are elaborately manipulated to make the etching rate of Ta₂O₅ match with the heterogeneous nucleation and crystal growth rate of NaTaO₃ by simply adjusting such parameters as the NaOH concentration ([NaOH]), solvent species. As a result, fragmentary NaTaO₃ nanocubes in-situ grow along [1 2 1] on the Ta₂O₅ (1 1 0) crystal planes to form facet-coupling heterojunctions. Importantly, owing to the effectively reduced interface defects and the minimum charge transfer resistance in the facet-coupling heterojunctions, the as-obtained facet-coupling heterostructured NaTaO₃/Ta₂O₅ porous nanofibers show an obviously enhanced interfacial charge separation and a significantly improved photocatalytic hydrogen production activity compared with the NaTaO₃/Ta₂O₅ composites, homogeneous Ta₂O₅ nanofibers and NaTaO₃ nanofibers. This is the first example of tantalum-based heterostructures with well-defined interfaces. The synchronous etching-growth strategy reported here will open a new era to manufacture well-defined heterojunctions.

2. Experimental

2.1. Catalyst preparation

The Ta₂O₅ nanofibers were prepared by the electrospinning method. 0.78 g tantalum ethoxide was added to a mixture of 4 g absolute ethanol and 1.5 g acetic acid in a capped bottle. Then 0.35 g PVP K90 was added to the solution and stirred at room temperature for 5 h to get a homogeneous viscous solution. Then the obtained solution was drawn into a plastic syringe equipped with a capillary. The feeding rate of the solution in the syringe was controlled as 400 μ L/h by using a syringe pump. The voltage connected to the needle of the syringe was 10 kV and the distance between the tip of the needle and the aluminum foil collector was 20 cm. Finally, the electrospun nanofibers were calcined in air at 740 °C for 1 h, and the heating rate was 10 °C/min.

The facet-coupling heterostructured NaTaO₃/Ta₂O₅ porous nanofibers were synthesized by the solvothermal method using Ta₂O₅ porous nanofibers as the precursors. In a typical synthesis, 40 mg Ta₂O₅ porous nanofibers were added in 75 mM, 45 mL NaOH solutions with ethanol/water ratio of 40:5 at room temperature under ultrasonic conditions. Then the obtained solution was transferred into a Teflon-lined autoclave, and the autoclave was sealed and heated to 200 °C for 12 h. After the autoclave cooled to the room temperature, the precipitate was collected and washed with deionized water and absolute ethanol for several times, respectively, and then dried in an oven at 60 °C for 1 h for further characterization. In order to study the formation process of the as-prepared samples, we also prepared contrastive samples obtained at different NaOH concentrations (0, 0.07, 0.1 and 0.5 M), different ethanol/water ratios (0:45, 15:30, 22.5:22.5 and 45:0) as well as different solvothermal times (1, 5 and 9 h), respectively. The contents of NaTaO₃ in the as-prepared composites were estimated according to the EDX analysis.

For comparison, the contrastive NaTaO₃/Ta₂O₅ composite nanofibers were prepared by a one-step direct electrospinning method. The obvious difference is that the precursor solution was composed of 0.78 g tantalum ethoxide, 4 g absolute ethanol and 1.5 g acetic acid, 0.08 g sodium acetate and 0.5 g DMF. Then 0.5 g PVP K90 was added to obtain a transparent solution. The following procedure was consistent with the preparation of Ta₂O₅ nanofibers.

2.2. Catalyst characterization

The X-ray diffraction (XRD) patterns of the samples were measured on a D/Max-RBX X-ray diffractometer (Rigaku, Japan) using Cu K α irradiation in the range of $10^\circ \leq 2\theta \leq 80^\circ$ at room temperature. Scanning electron microscopy (SEM) and energy dispersive X-ray (EDX) analyses were obtained using a Hitachi S-4800 Field-emission SEM (Japan). Transmission electron microscopy (TEM) and high-resolution transmission electron microscopy (HRTEM) were carried out on a H-600 STEM/EDX (PV9100, HITACHI). Samples for TEM and HRTEM were ultrasonically dispersed in absolute ethanol, and the obtained suspension was dropped on a copper grid coated with carbon film and then drying in air. UV–vis diffuse reflectance spectra (DRS) of the samples were obtained on a UV-2550 UV–vis spectrophotometer (Shimadzu, Japan). BaSO₄ was used as a reflectance standard, and the spectra were recorded in the range 200–800 nm. Photoluminescence (PL) spectra were measured at room temperature on an F-7000 fluorescence spectrophotometer (Hitachi, Japan) with an excitation wavelength of 320 nm.

2.3. Photocatalytic activity tests

The photocatalytic activities for hydrogen production of the samples were evaluated without any cocatalysts under the simulant solar light irradiation in pure water and 20 vol% methanol aqueous solutions, respectively. The reactions were carried out in a sealed gas circulation system with an external irradiation cell. The reactor was placed about 20 cm under a 300 W xenon lamp (PLS-SXE300, Beijing Trusttech Co., Ltd., China). This lamp shows a spectrum covering from 320 nm to 780 nm with the UV output power of 2.6 W and the visible output power of 19.6 W, and can act as a simulant solar light source. The detailed process was as follows: 20 mg of the as-prepared catalysts were ultrasonically dispersed for 30 min in 100 mL pure water or 20 vol% methanol aqueous solutions. After the closed gas circulation system and reaction cells were well evacuated, the suspension was irradiated by the simulant solar light, and the solution was kept under stirring with a magnetic stirrer during reaction in order to prohibit particles to settle at the bottom of the reactor. Meanwhile, after 1 h internal of irradiation, the evolved gases were in situ analyzed by a gas chromatograph (TECHCOMP, GC 7890-II, MS-5A column, nitrogen carrier), which was connected directly to the closed gas circulating line.

2.4. Electrochemical measurements

Electrochemical impedance spectra (EIS) were measured using an electrochemical analyzer (CHI760D) in a conventional three-electrode cell in the electrolyte of 0.5 M H₂SO₄ aqueous solution. Platinum foil and a saturated calomel electrode (SCE) were used as the counter electrode and the reference electrode, respectively. For preparing working electrode, 80 mg sample was mixed with 1 mL H₂O and 100 μ L poly(vinyl alcohol) (PVA) adhesive by ultrasonication for 20 min. The PVA adhesive was prepared by mixing 2.5 g PVA and 50 mL H₂O at 50 °C for 10 h and subsequently at 90 °C for 5 h. Then 100 μ L of the mixture was spread onto the carbon cloth and dried under an infrared heat lamp. This process was repeated for twice to obtain the working electrode. The working electrode exposed to the electrolyte was a circular film with a surface area of 0.2 cm².

3. Results and discussion

We have synthesized the facet-coupling heterostructured NaTaO₃/Ta₂O₅ porous nanofibers by a solvothermal method using Ta₂O₅ porous nanofibers as the precursor. The typical sample was

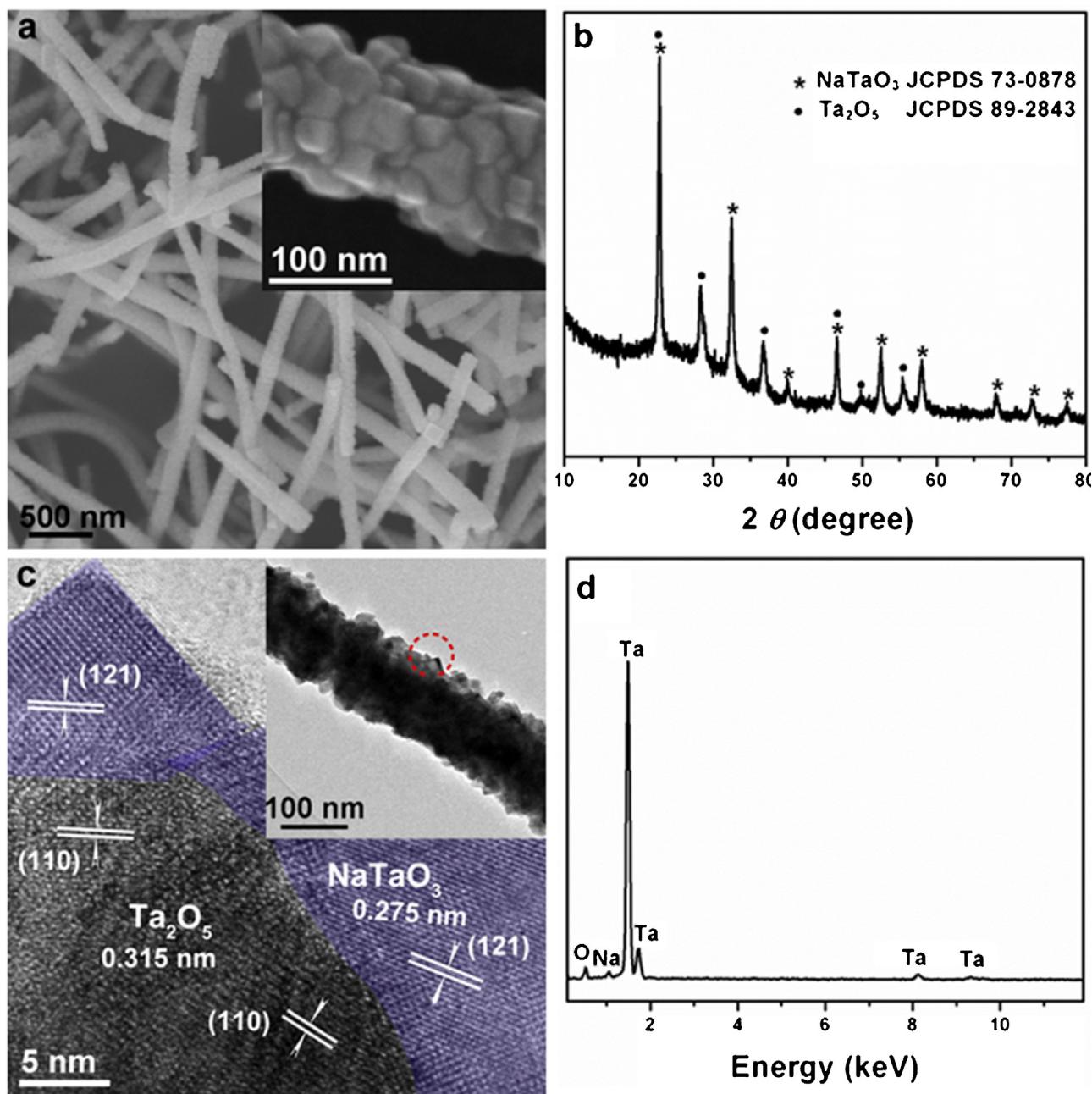


Fig. 1. (a) SEM images, (b) XRD pattern, (c) TEM and HRTEM images, and (d) EDX analysis of the obtained typical facet-coupling heterostructured NaTaO₃/Ta₂O₅ nanofibers.

Table 1

The contents and crystallite sizes of NaTaO₃ in the samples obtained at different solvothermal conditions.

Entry	[NaOH] (M)	$V_{\text{ethanol}}/V_{\text{water}}$	t (h)	Product	NaTaO ₃ % (mol.%)	D_p^a (nm)
1	0	40/5	12	Ta ₂ O ₅ nanofibers	0	0
2	0.07	40/5	12	NaTaO ₃ /Ta ₂ O ₅ nanofibers	56	18.5
3	0.075	40/5	12	NaTaO ₃ /Ta ₂ O ₅ nanofibers	69	19.4
4	0.1	40/5	12	NaTaO ₃ /Ta ₂ O ₅ nanofibers	85	19.8
5	0.5	40/5	12	NaTaO ₃ nanofibers composed of nanocubes	100	24.8
6	0.5	0/45	12	NaTaO ₃ nanocubes	100	–
7	0.075	0/45	12	Ta ₂ O ₅ nanofibers	0	–
8	0.075	15/30	12	NaTaO ₃ /Ta ₂ O ₅ nanofibers	15	–
9	0.075	22.5/22.5	12	NaTaO ₃ /Ta ₂ O ₅ nanofibers	62	–
10	0.075	45/0	12	NaTaO ₃ /Ta ₂ O ₅ nanofibers	25	–
11	0.075	45/0	20	NaTaO ₃ /Ta ₂ O ₅ nanofibers	29	–
12	0.075	40/5	1	NaTaO ₃ /Ta ₂ O ₅ nanofibers	52	16.1
13	0.075	40/5	5	NaTaO ₃ /Ta ₂ O ₅ nanofibers	62	18.4
14	0.075	40/5	9	NaTaO ₃ /Ta ₂ O ₅ nanofibers	65	19.0

^a D_p is the crystallite size of NaTaO₃ estimated by the Debye–Scherrer formula on the basis of the full width at half maximum of (1 2 1) XRD diffraction peaks.

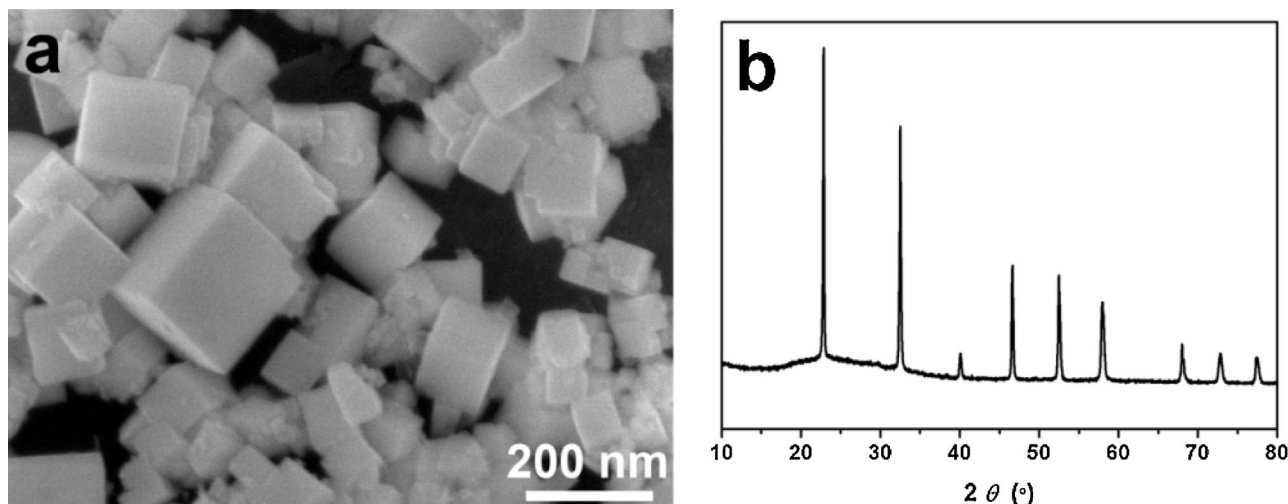


Fig. 2. SEM image (a) and XRD pattern (b) of the sample obtained in 0.5 M NaOH aqueous solution.

obtained in a 75 mM NaOH solution with ethanol/water ratio of 40:5. The SEM image in Fig. 1a reveals that the as-obtained product is entirely composed of nanofibers with a uniform diameter of 100 ± 5 nm and a well-defined shape. The inset of Fig. 1a shows that the nanoparticles covered on the surface of nanofibers have shaped edges with right-angles. This is quite different from the morphology of the electrospun Ta_2O_5 nanofibers, implying the formation of a new component in the as-prepared product. The XRD diffraction peaks in Fig. 1b can be readily indexed to orthorhombic NaTaO_3 (space group $Pcmn$ (No. 62)) with lattice constants $a = 5.5213$ Å, $b = 7.7952$ Å and $c = 5.4842$ Å (JCPDS 73-0878) and orthorhombic Ta_2O_5 (space group $C2/m$ (No. 38)) with lattice constants $a = 6.2$ Å, $b = 3.66$ Å and $c = 3.89$ Å (JCPDS 89-2843), revealing that the as-prepared product consists of NaTaO_3 and Ta_2O_5 . The HRTEM image (Fig. 1c) further indicates that the fragmentary NaTaO_3 nanocubes grows along [1 2 1] on the Ta_2O_5 (1 1 0) crystal planes, forming a tight and compact heterostructure. This is because in this case, the lattice mismatch between the crystal plane of NaTaO_3 (1 2 1) and that of Ta_2O_5 (1 1 0) $\delta = 2|a_{(121)} - a_{(110)}|/a_{(121)} + a_{(110)}$ (where $a_{(121)}$ and $a_{(110)}$ correspond to their interplanar spacings) is calculated to be only about 13%, much lower than those of the other cases. The irregular distribution of NaTaO_3 nanocubes on the surface of nanofibers can be ascribed to the randomly exposed (1 1 0) crystal planes of Ta_2O_5 nanoparticles in the electrospun Ta_2O_5 nanofibers. The facet-coupling character of the as-prepared sample has been further confirmed by more similar HRTEM images taken from other heterostructures between NaTaO_3 and Ta_2O_5 (Fig. S1). Fig. 1d shows the EDX analysis of the as-obtained typical facet-coupling heterostructured $\text{NaTaO}_3/\text{Ta}_2\text{O}_5$ nanofibers. It indicates that the sample contains Na, Ta, and O elements. The atomic ratio of Na and Ta elements in the sample is 1:1.9. Thus, the NaTaO_3 content in the as-obtained heterostructures can be calculated to be 69 mol.%. The above characterization clearly suggests that using the synchronous etching-growth technology has obtained the facet-coupling heterojunctions between the NaTaO_3 (1 2 1) crystal planes and the Ta_2O_5 (1 1 0) crystal planes, which can effectively reduce the interface defects and minimize the charge transfer resistance, and thus are expected to enhance the photocatalytic activity for hydrogen production.

To decipher the formation process of the as-prepared facet-coupling heterostructured $\text{NaTaO}_3/\text{Ta}_2\text{O}_5$ nanofibers, the solvothermal conditions influencing on the structures and morphologies of the products have been in detail investigated including the NaOH concentration ([NaOH]), solvent species and solvother-

mal time (t), etc., and the corresponding data are listed in Table 1. Figs. S2 and S3 show the SEM images and XRD patterns of the products prepared at different [NaOH]. It can be seen that only in the presence of NaOH can the $\text{NaTaO}_3/\text{Ta}_2\text{O}_5$ composite nanofibers be obtained, and the contents and average crystallite sizes of NaTaO_3 nanocubes increase with increasing [NaOH]. When [NaOH] is up to 0.5 M, NaTaO_3 nanofibers which are entirely composed of nanocubes are prepared. These results indicate that the generation of NaTaO_3 during the solvothermal process is closely related to the concentration of free OH^- anions.

The results of experiment 6 in Table 1 states that when the mixed solvent is replaced with water containing 0.5 M NaOH, the Ta_2O_5 nanofibers are completely etched, forming separated NaTaO_3 nanocubes, as shown in Fig. 2. This means that the etching of Ta_2O_5 nanofibers in pure water is completed before the generation of NaTaO_3 nanocubes, indicating a rapid reaction rate of Ta_2O_5 nanofibers with NaOH in water. The effect of the ratio of ethanol/water on the formation of the as-prepared $\text{NaTaO}_3/\text{Ta}_2\text{O}_5$ composite nanofibers is further studied shown in Fig. S4 and experiments 7–10 in Table 1. At [NaOH] of 75 mM, the reaction of free OH^- ions with Ta_2O_5 nanofibers does not occur to generate alkaline hydroxylated Ta-O ionic groups in water, whereas it happens under the solvothermal condition. This is because the free OH^- ions in ethanol aqueous solution exhibit a higher activity than those in water due to the weak solvation of ethanol [20–22]. The extraordinary decrease of the NaTaO_3 content in ethanol suggests that the existence of a small amount of water can accelerate the etching of Ta_2O_5 nanofibers. The decreased etching rate in the presence of ethanol can also be evidenced by experiment 11 in Table 1, where the content of NaTaO_3 in the product increased slightly to 29% even when t is prolonged to 20 h. Therefore, it is vital for the formation of facet-coupling heterostructured $\text{NaTaO}_3/\text{Ta}_2\text{O}_5$ nanofibers to have an etching rate of Ta_2O_5 nanofibers matching with the heterogeneous nucleation and crystal growth rate of NaTaO_3 , which is determined by the free OH^- ions activity and an appropriate reaction rate.

Fig. 3 shows the effect of t on the product structures. Combining with the data in experiments 12–14 of Table 1, we can easily found that in the first 1 h, the solvothermal reaction shows a high reaction rate and many obvious nanocubes are generated on the surface of nanofibers, indicating the etching of Ta_2O_5 begins with the surface of nanofibers. With prolonging t , the content and crystallite sizes of the NaTaO_3 increase accordingly with a small degree. The increase is mainly due to the fact that when the surficial Ta_2O_5 nanoparticles

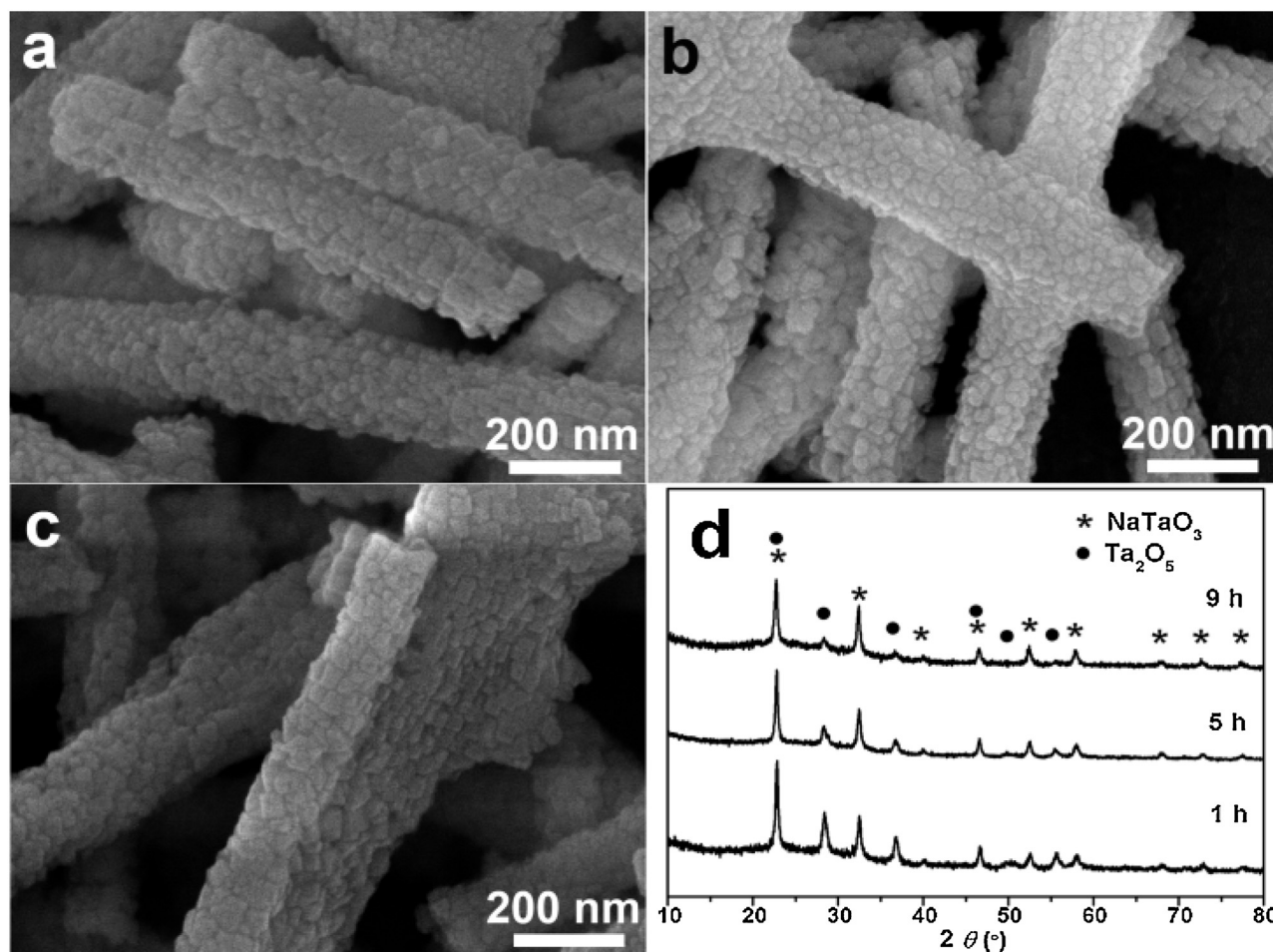


Fig. 3. SEM images of the samples obtained at different reaction time (t) of (a) 1 h, (b) 5 h and (c) 9 h, as well as their corresponding XRD patterns (d).

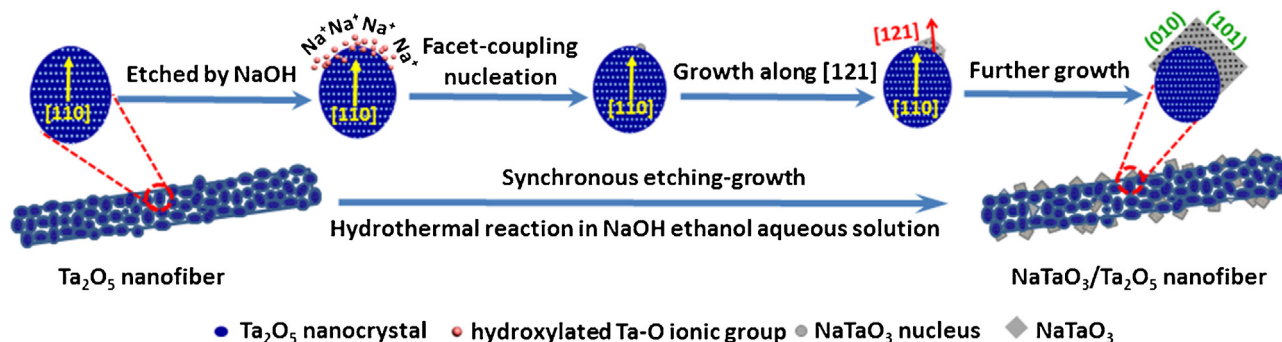
have been etched, the rate of the solvothermal reaction depends on the mass transport or diffusion of the free OH^- ions into the inner of nanofibers. Therefore, it is vital for the in-situ epitaxial growth of facet-coupling heterostructured $\text{NaTaO}_3/\text{Ta}_2\text{O}_5$ nanofibers that deliberately controlling the concentration of higher active and free OH^- anions and the solvent composition makes the dissolution rate of Ta_2O_5 match with the nucleation and crystal growth rates of NaTaO_3 .

Based on the effects of the solvothermal conditions on the structures and morphologies of the products described in the above, we can reasonably propose the formation mechanism of the as-obtained facet-coupling heterostructured $\text{NaTaO}_3/\text{Ta}_2\text{O}_5$ nanofibers in Scheme 1. In the solvothermal process, the electrospun Ta_2O_5 nanofibers are partly etched from the surface and hydroxylated by the free OH^- ions to form a variety of hydroxylated Ta–O ionic groups under strongly alkaline conditions [14,23]. When the Na^+ ions and hydroxylated Ta–O ionic groups in the solution around the Ta_2O_5 grains reach the super saturated concentration, the NaTaO_3 begins to nucleate on the surface of the etched Ta_2O_5 nanoparticles. With the etching reaction continuing to form more hydroxylated Ta–O ionic groups, the in-situ epitaxial growth of stable NaTaO_3 nanograins occurs along (1 1 0) plane of the etched Ta_2O_5 nanoparticles due to the lowest lattice mismatch with the (1 2 1) plane of NaTaO_3 . As the (1 2 1) plane of NaTaO_3 has the fastest growth rate, it will disappear quickly with the reaction continuing, making the mutually perpendicular (0 2 0) and (1 0 1) planes of NaTaO_3 with the same interplanar spacing (0.389 nm) exposed to form nanocubes [14,23]. In such a way, we have for the first time

obtained a facet-coupling heterostructure based on Ta_2O_5 . This heterojunction is completely different from the previously reported heterostructured Ta_2O_5 -based photocatalysts, in which the crystal planes of the different components contact randomly, even are separated by an amorphous transition [15,16,24].

Furthermore, in order to evaluate the advantage of the as-prepared facet-coupling heterostructured $\text{NaTaO}_3/\text{Ta}_2\text{O}_5$ porous nanofibers in the light absorption, charge transfer and photocatalytic hydrogen production, we have also synthesized the $\text{NaTaO}_3/\text{Ta}_2\text{O}_5$ composite nanofibers with the same NaTaO_3 content as that of the as-obtained facet-coupling heterostructured $\text{NaTaO}_3/\text{Ta}_2\text{O}_5$ by a one-step approach for comparison. Fig. 4 shows the SEM image and XRD pattern of the $\text{NaTaO}_3/\text{Ta}_2\text{O}_5$ composite nanofibers. It is clear that the contrastive $\text{NaTaO}_3/\text{Ta}_2\text{O}_5$ composite exhibits a nanofiber morphology with a rough and porous surface, which is different from the as-prepared facet-coupling heterostructure.

Fig. 5 shows the UV–vis spectrum of the as-obtained facet-coupling heterostructured $\text{NaTaO}_3/\text{Ta}_2\text{O}_5$ nanofibers. For comparison, the UV–vis spectra of the homogeneous counterparts, such as the Ta_2O_5 nanofibers and NaTaO_3 nanofibers, as well as the contrast samples of the $\text{NaTaO}_3/\text{Ta}_2\text{O}_5$ composite nanofibers characterized in Fig. 4 are also depicted here. Simultaneously, the corresponding bandgap energies of the four samples have been estimated by the Kubelka–Munk method (the inset of Fig. 5). As shown in Fig. 5, the light absorption band edges of the pristine Ta_2O_5 nanofibers and NaTaO_3 nanofibers appear at 326 and 347 nm, respectively, corresponding to the bandgap energies of



Scheme 1. The illustration for the formation mechanism of the as-prepared facet-coupling heterostructured NaTaO₃/Ta₂O₅ nanofibers.

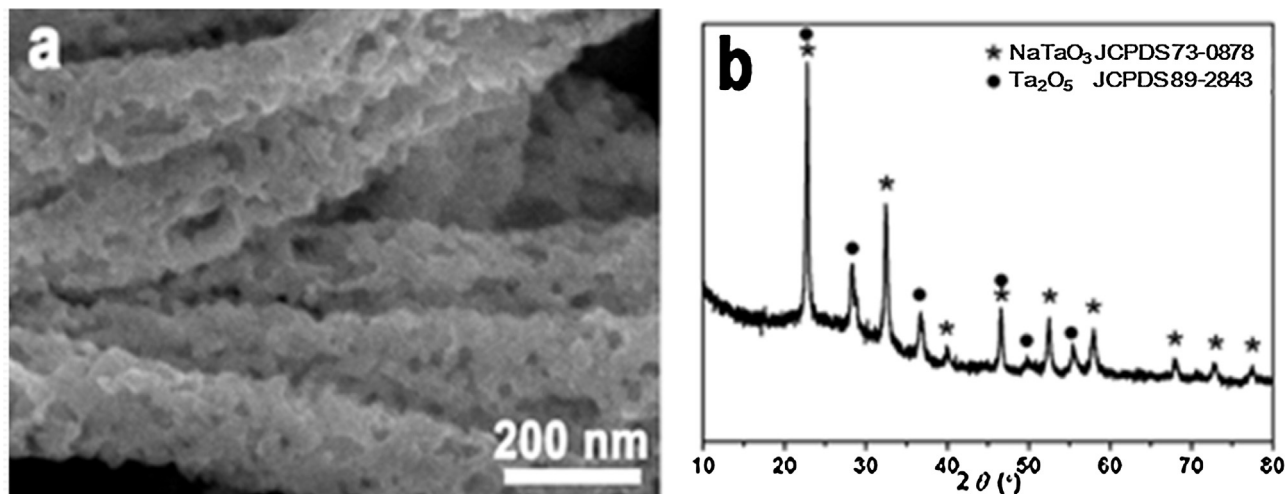


Fig. 4. SEM image (a) and XRD pattern (b) of the NaTaO₃/Ta₂O₅ composite nanofibers prepared by a one-step direct electrospinning method.

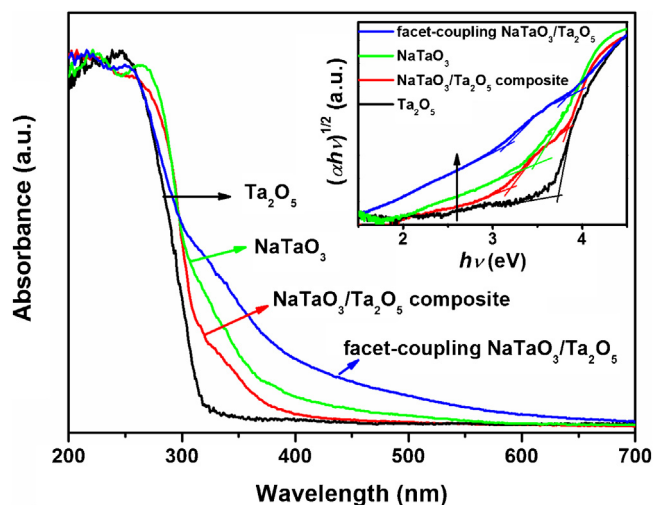


Fig. 5. UV-vis DR spectra of the as-prepared facet-coupling heterostructured NaTaO₃/Ta₂O₅ nanofibers, as well as the Ta₂O₅, NaTaO₃ and NaTaO₃/Ta₂O₅ composites. The inset is the corresponding plot of $(\alpha h\nu)^{1/2}$ versus energy ($h\nu$) for the band gap energies.

3.80 and 3.57 eV. These are attributed to their intrinsic absorptions. For the as-prepared facet-coupling and composite heterostructures, they both exhibit two distinctive band edges. These are both ascribed to the electron band-to-band transition energies of Ta₂O₅ and NaTaO₃, respectively, further indicating their compositions. But the as-prepared facet-coupling heterostructures exhibit a

much stronger light absorption than the NaTaO₃/Ta₂O₅ composite nanofibers even when they have similar chemical compositions. On the other hand, the nanofibers composed of pristine NaTaO₃ nanocubes have also a light absorption band edge at 347 nm, corresponding to the bandgap energies (E_g) of 3.57 eV. These two values are somewhat different from the corresponding ones of the NaTaO₃ microparticles reported by the Kudo's group, which have an absorption band edge at 310 nm and E_g of 4.0 eV [25]. The as-prepared NaTaO₃ nanofibers show an obvious red-shift in the absorption band edge with a narrower band gap if compared with the latter. This is because the latter samples are prepared by an entirely different solid-state method. They have different structures and morphologies from the NaTaO₃ nanofiber samples fabricated here, and thus exhibit somewhat different light absorption regions. This similar phenomenon has also been reported in some other materials, such as Ta₂O₅ and CdS, etc. [26–29]. For example, commercial Ta₂O₅ has a band gap of 4.0 eV, while the amorphous mesoporous Ta₂O₅ prepared by a sol-gel method shows a light absorption band edge of 320 nm, corresponding to the band gap of ~3.88 eV. In comparison, Fig. 5 indicates that the as-prepared Ta₂O₅ nanofibers have a red-shift band edge at 326 nm, which corresponds to a relative narrow band gap of 3.8 eV. This clearly suggests that the semiconductor materials fabricated by different synthesis methods may exhibit a variety of light absorption properties and energy band structures.

Fig. 6 displays the photocatalytic activities for hydrogen production from 20 vol% methanol aqueous solution and pure water of the as-prepared facet-coupling heterostructured NaTaO₃/Ta₂O₅ nanofibers, as well as the Ta₂O₅ nanofibers, the NaTaO₃/Ta₂O₅ composite nanofibers prepared by a one-step electrospinning method,

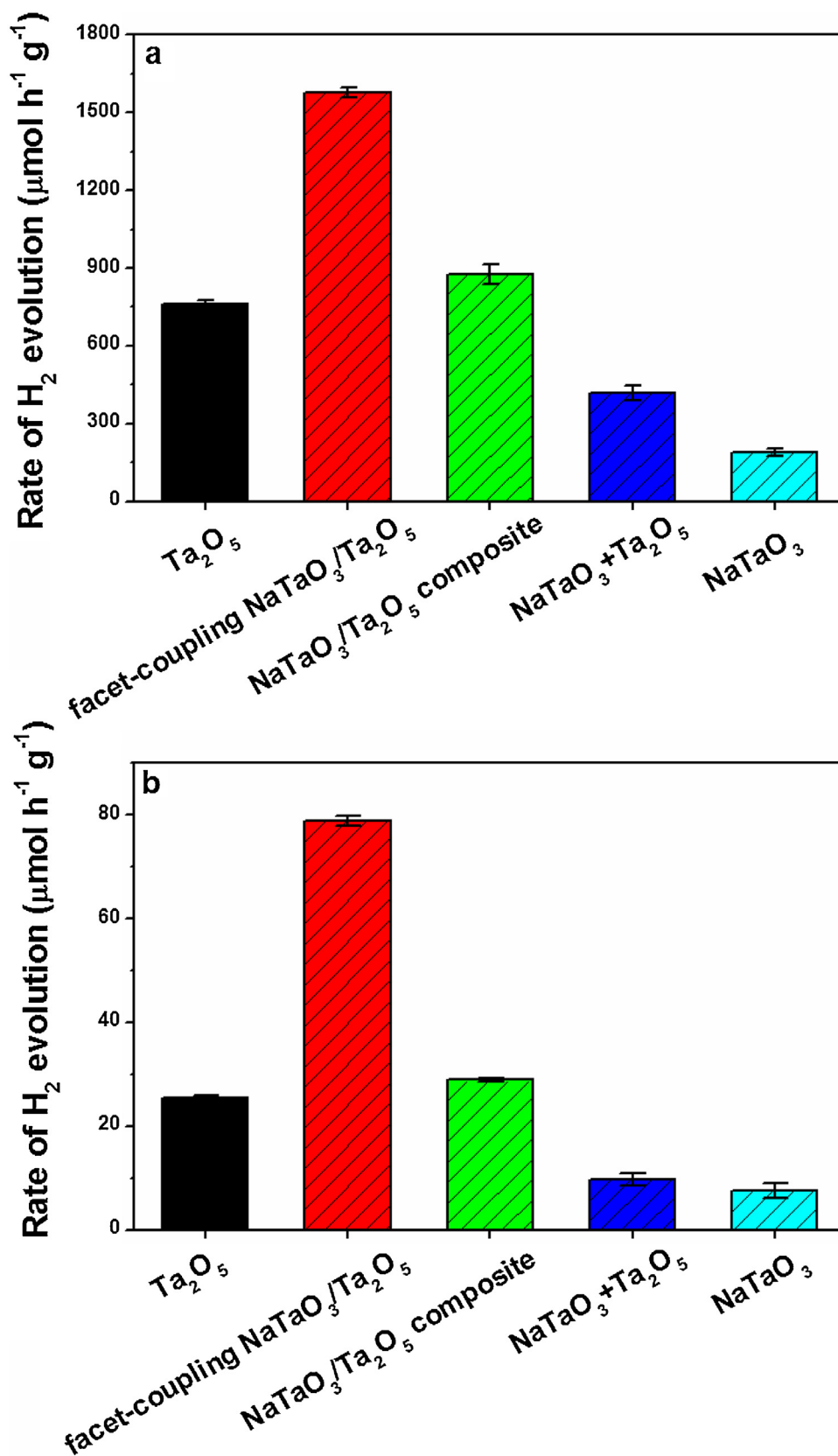


Fig. 6. Photocatalytic activities for hydrogen production from 20 vol% methanol aqueous solution (a) and pure water (b) of the as-prepared facet-coupling heterostructured NaTaO₃/Ta₂O₅ nanofibers, as well as the Ta₂O₅ nanofibers, the NaTaO₃/Ta₂O₅ composite nanofibers prepared by one-step method, the mechanically mixed sample of NaTaO₃ and Ta₂O₅ nanofibers and the NaTaO₃ nanofibers under simulant solar light irradiation.

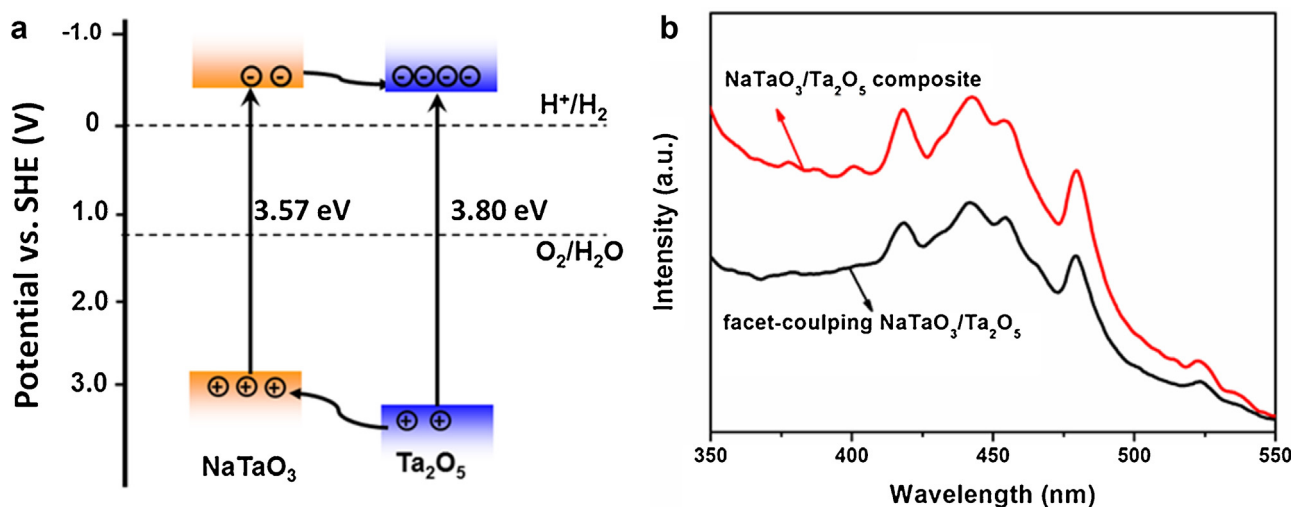


Fig. 7. (a) PL spectra of the as-prepared facet-coupling NaTaO₃/Ta₂O₅ nanofibers and NaTaO₃/Ta₂O₅ composite nanofibers; (b) Illustration of photogenerated charge separation and transfer in the NaTaO₃/Ta₂O₅ heterostructures.

the mechanically mixed sample of NaTaO₃ and Ta₂O₅ nanofibers and the NaTaO₃ nanofibers under simulant solar light irradiation. From Fig. 6a, it can be easily observed that among all the tested photocatalytic materials, the as-prepared facet-coupling heterostructured NaTaO₃/Ta₂O₅ nanofibers exhibit the highest photocatalytic activity of 1579 $\mu\text{mol h}^{-1} \text{g}^{-1}$ without any cocatalysts, which is 3.1 times larger than that of Ta₂O₅ nanofibers, and 10.5 times as large as that of NaTaO₃ nanofibers. This is in sharp contrast with the fact that most of the photocatalytic materials reported so far usually require the participation of expensive cocatalysts (NiO and Pt, etc.) to acquire high photocatalytic activities for hydrogen production [24,30–33], and implies a possibility that well-defined heterostructures do not need the modification of cocatalysts. Fig. 6b shows the photocatalytic activities for hydrogen production in water of all tested samples. The trend is similar to that obtained in methanol aqueous solution and the as-prepared facet-coupling heterostructured NaTaO₃/Ta₂O₅ nanofibers also exhibits the highest photocatalytic hydrogen production efficiency.

In order to clear the origin of the enhanced photocatalytic activity, the BET surface areas of the facet-coupling heterostructured NaTaO₃/Ta₂O₅ nanofibers and the contrastive NaTaO₃/Ta₂O₅ composite nanofibers are estimated, respectively, to be 10.7 and 16.0 $\text{m}^2 \text{g}^{-1}$ by N₂ adsorption-desorption analysis (Fig. S5). The facet-coupling heterostructured NaTaO₃/Ta₂O₅ nanofibers exhibits the far higher photocatalytic activity than that of NaTaO₃/Ta₂O₅ composite nanofibers, even though it has the smaller surface area. The result sufficiently illustrates that besides surface area, the reduced interface defects and the minimum charge transfer resistance of the as-prepared facet-coupling heterostructures for effective charge separation are the essential factors for enhanced photocatalytic hydrogen production.

According to the previous reports, the conduction band (CB) bottom of NaTaO₃ is slightly higher than that of Ta₂O₅ [34–36]. Under simulant solar light irradiation the photogenerated electrons located on the CB bottom of NaTaO₃ can transfer to the CB of Ta₂O₅ because of the potential gradient shown in Fig. 7a. This greatly enhances the charge separation efficiencies and prolongs the lifetime of the photogenerated charge carriers of the two heterostructures. As a consequence, both the facet-coupling and composite heterostructures exhibit relatively high photocatalytic activities compared with single Ta₂O₅ and NaTaO₃ as well as the mechanically mixed sample. For the two

heterostructures, their charge separation behaviors are characterized by the photoluminescence (PL) emission spectra (Fig. 7b) since PL emission results from their recombination [37–39]. Compared with the contrast NaTaO₃/Ta₂O₅ composite nanofibers, the as-prepared facet-coupling heterostructures exhibit a lower PL emission intensity, suggesting that the as-prepared facet-coupling heterostructures have a relatively low recombination rate of photogenerated electrons and holes. As these two kinds of samples are the same except from the interface structures, it can be reasonably inferred that the facet-coupling interfaces benefit the acceleration of the charge transfer from NaTaO₃ to Ta₂O₅, resulting in the further enhancement of the charge separation efficiency of heterostructures because of the effectively reduced interface defects and the minimum charge transfer resistance.

The charge transfer process of the facet-coupling heterostructured NaTaO₃/Ta₂O₅ nanofibers is analyzed by the electrochemical impedance spectroscopy (EIS). For comparison, the contrastive NaTaO₃/Ta₂O₅ composite and NaTaO₃ nanofibers are also characterized. Fig. 8a shows the Bode plots of the three samples. It can be clearly observed that the resistances decrease gradually and the phase angles exhibit three peaks with the increment of frequencies from 1 to 10⁶ Hz. The Bode magnitude plots are remarkably different in the frequency region from 10¹ to 10⁴ Hz. Since the three working electrodes all consist of the same carbon cloth but with different samples, this dramatic difference among the resistances suggests the different charge transfer process of the samples, which can be further verified by the fitting results of the corresponding equivalent circuit model. The occurrence of the three peaks in the Bode phase angle plots (the inset of Fig. 8a) implies that the samples all have three time constants when frequency is increased from 1 to 10⁶ Hz. As each time constant implies a charge transfer process and is represented by a resistance capacitance (RC) parallel circuit [40,41], an equivalent circuit model can be reasonably proposed, as shown in the inset of Fig. 8b. Hereinto, R_s is the solution resistance. R₁ and C₁ stand for the resistance and double layer capacitance at the electrolyte/sample interface. R₂ and CPE represent the charge transport resistance and the chemical capacitance of the as-prepared samples, while R₃ and C₂ imply the resistance and capacitance at the sample/electrode interface. Using this equivalent circuit model to statistically fit the Nyquist plots in Fig. 8b, the charge transfer resistances (R₂) of the as-prepared facet-coupling NaTaO₃/Ta₂O₅ nanofibers and NaTaO₃/Ta₂O₅ com-

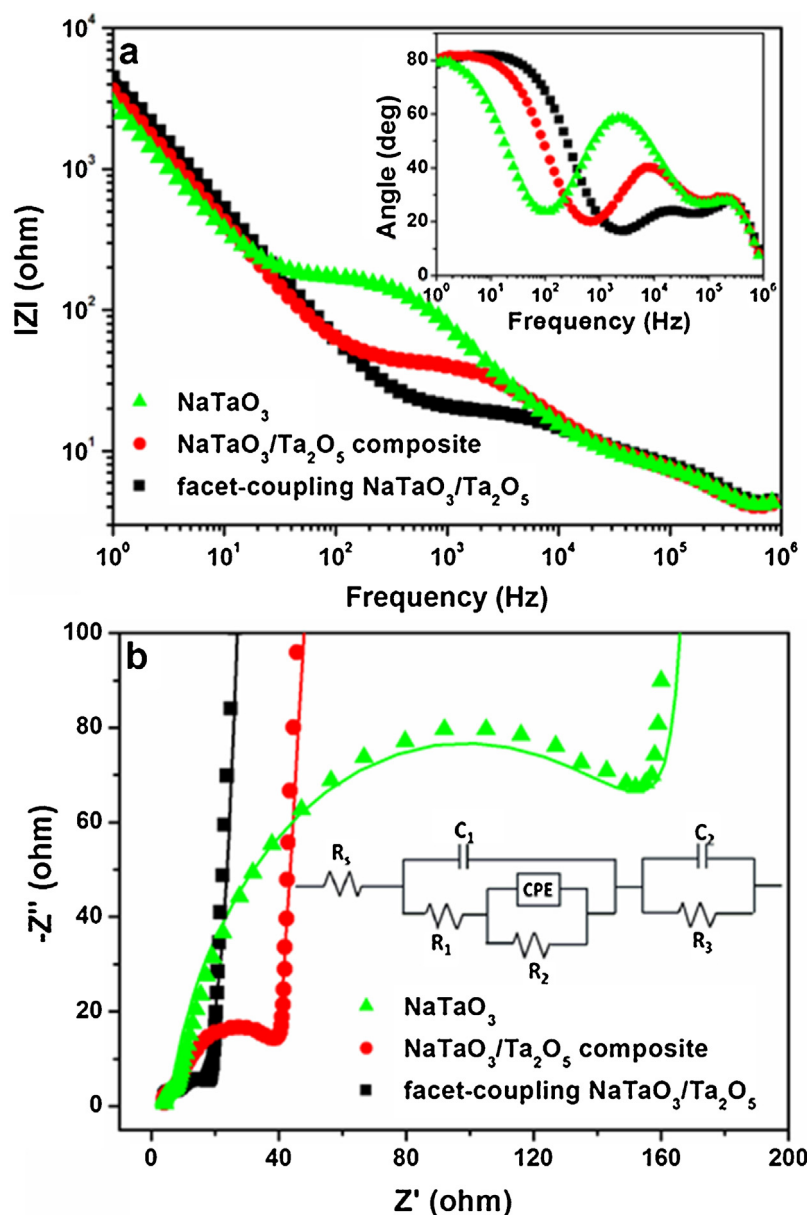


Fig. 8. EIS Bode (a) and Nyquist (b) plots of the as-prepared facet-coupling NaTaO₃/Ta₂O₅ nanofibers and the NaTaO₃/Ta₂O₅ composite nanofibers as well as NaTaO₃. The inset of b is the equivalent circuit model for EIS modeling. Solid lines show the fitting curves.

posite nanofibers as well as NaTaO₃ nanofibers are calculated to be 10.7, 33.4 and 162.1 ohm, respectively. The smallest R_2 of the facet-coupling NaTaO₃/Ta₂O₅ nanofibers indicates its more efficient charge transfer than those of NaTaO₃/Ta₂O₅ composite nanofibers and NaTaO₃. This can be well explained by the well-fabricated interfacial structure of the facet-coupling NaTaO₃/Ta₂O₅ nanofibers, which is able to provide more effective electron pathways and decrease the charge transfer resistance, and thus further enhance the photocatalytic efficiencies of heterostructures [42,43].

Fig. 9 shows the stability of the as-prepared facet-coupling heterostructured NaTaO₃/Ta₂O₅ nanofibers in 20 vol% methanol aqueous solution under simulant solar light irradiation. Obviously, the decrease in the photocatalytic activity for hydrogen production is undiscernible in our experiment, indicating that the as-prepared facet-coupling NaTaO₃/Ta₂O₅ heterostructured photocatalyst exhibits a good long-term stability. This is because besides the good chemical stability and photochemical inertness of both NaTaO₃ and Ta₂O₅, the electron acceptor Ta₂O₅ cannot be

reduced by the transferred electrons due to its much lower reduction potential (−0.75 V).

4. Conclusions

In summary, we have developed a synchronous etching-epitaxial growth approach for the fabrication of facet-coupling heterostructured NaTaO₃/Ta₂O₅ porous nanofibers by regulating the etching rate of Ta₂O₅ nanofibers to match with the heterogeneous nucleation and growth rate of NaTaO₃ nanocubes. In the as-prepared facet-coupling heterostructured NaTaO₃/Ta₂O₅ porous nanofibers, the fragments of NaTaO₃ nanocubes uniformly grow along [121] on the Ta₂O₅ (110) crystal plane under a solvothermal condition. Compared to the traditional heterostructures with crystal planes of the semiconducting components randomly contacting, the as-prepared facet-coupling heterostructured NaTaO₃/Ta₂O₅ nanofibers have an intrinsic advantage of much low lattice mismatch. The as-prepared facet-coupling het-

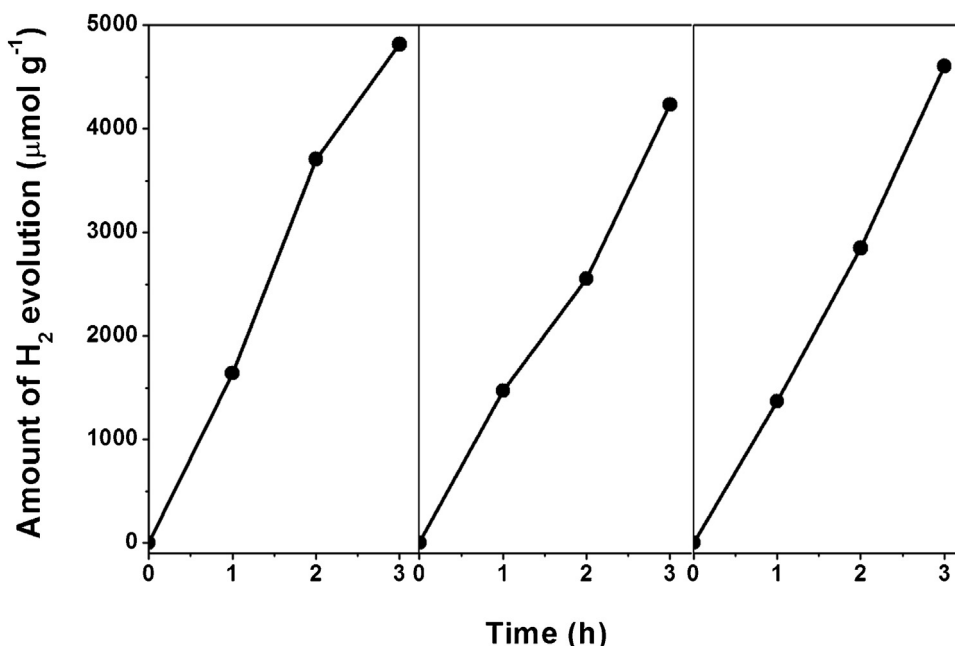


Fig. 9. The stability for photocatalytic hydrogen evolution of the as-prepared facet-coupling heterostructured NaTaO₃/Ta₂O₅ nanofibers in each 3 h under simulant solar light irradiation.

erostructures have reduced interface defects and a minimized charge transfer resistance. Consequently, the as-prepared facet-coupling heterostructures not only exhibit an increased light absorption capacity, but also an accelerated charge transfer between the interfaces, leading to an enhanced photocatalytic activity and stability for hydrogen production without any co-catalysts under the simulant solar light irradiation. It is the first time to concentrate on the regulation of interfacial structures of heterostructures, which promises a reliable way to achieve the improvement of photoinduced charge separation and the acceleration of charge transfer for photocatalysis, photoelectrochemistry and electrochemistry. The synchronous etching-epitaxial growth approach reported here provides a simple and feasible approach to fabricate semiconductor–semiconductor heterostructures with coupled crystalline facets in a liquid phase.

Acknowledgements

This work was financially supported by the National Natural Science Foundation of China (51002111 and 51521001), the Natural Science Foundation of Hubei Province (2014CFB163 and 2015CFA003), the Top Talents Lead Cultivation Project of Hubei Province, the Yellow Crane talent plan of Wuhan municipal government and the Fundamental Research Funds for the Central Universities (WUT: 2014-IV-131).

Appendix A. Supplementary data

Supplementary data associated with this article can be found, in the online version, at <http://dx.doi.org/10.1016/j.apcatb.2015.11.041>.

References

- [1] D.J. Milliron, S.M. Hughes, Y. Cui, L. Manna, J. Li, L.W. Wang, A.P. Alivisatos, *Nature* 430 (2004) 190–195.
- [2] A.K. Giri, C. Charan, A. Saha, V.K. Shahi, A.B. Panda, *J. Mater. Chem. A* 2 (2014) 16997–17004.

- [3] F.P. Peng, Q. Zhou, D.P. Zhang, C.H. Lu, Y.R. Ni, J.H. Kou, J. Wang, Z.Z. Xu, *Appl. Catal. B: Environ.* 165 (2015) 419–427.
- [4] M. Niu, F. Huang, L. Cui, P. Huang, Y. Yu, Y. Wang, *ACS Nano* 4 (2010) 681–688.
- [5] S. Fujita, H. Kawamori, D. Honda, H. Yoshida, M. Arai, *Appl. Catal. B: Environ.* 181 (2016) 818–824.
- [6] A. Moya, A. Cherevan, S. Marchesan, P. Gebhardt, M. Prato, D. Eder, J.J. Vilatela, *Appl. Catal. B: Environ.* 179 (2015) 574–582.
- [7] R. Marschall, *Adv. Funct. Mater.* 24 (2014) 2421–2440.
- [8] W. Guo, Y.X. Yang, Y.N. Guo, Y.Q. Jia, H.B. Liu, Y.H. Guo, *Phys. Chem. Chem. Phys.* 16 (2014) 2705–2714.
- [9] Y.L. Min, G.Q. He, Q.J. Xu, Y.C. Chen, *J. Mater. Chem. A* 2 (2014), 2758–2584.
- [10] A.S. Pratt, P.R. Smith, Google Patents, 1989.
- [11] F. Holleman, E. Wiberg, N. Wiberg, *Lehrbuch der Anorganischen Chemie*, Walter de Gruyter, 1995.
- [12] F. Fairbrother, *The Chemistry of Niobium and Tantalum*, Elsevier, Amsterdam, 1967.
- [13] H.Y. Yang, S.F. Yu, S.P. Lau, X. Zhang, D.D. Sun, G. Jun, *Small* 5 (2009) 2260–2264.
- [14] X. Li, J. Zang, *J. Phys. Chem. C* 113 (2009) 19411–19418.
- [15] L.L. Xu, J.G. Guan, W.D. Shi, *ChemCatChem* 4 (2012) 1353–1359.
- [16] L.L. Xu, J.G. Guan, W.D. Shi, L.J. Liu, *J. Colloid Interface Sci.* 377 (2012) 160–168.
- [17] K.H. Reddy, S. Martha, K.M. Parida, *RSC Adv.* 2 (2012) 9423–9436.
- [18] H. Kato, A. Kudo, *Chem. Phys. Lett.* 295 (1998) 487–492.
- [19] J.Y. Duan, W.D. Shi, L.L. Xu, G.Y. Mou, Q.L. Xin, J.G. Guan, *Chem. Commun.* 48 (2012) 7301–7303.
- [20] A.D. McNaught, A. Wilkinson, *Compendium of Chemical Terminology*, Blackwell Science, Oxford, 1997.
- [21] L. Epshtein, A. Iogansen, *Russ. Chem. Rev.* 59 (1990) 134–151.
- [22] K.M. Dyumaev, B. Korolev, *Russ. Chem. Rev.* 49 (1980) 1021–1032.
- [23] T.G. Xu, X. Zhao, Y.F. Zhu, *J. Phys. Chem. B* 110 (2006) 25825–25832.
- [24] P. Zhang, J. Zhang, J. Gong, *Chem. Soc. Rev.* 43 (2014) 4395–4422.
- [25] H. Kato, A. Kudo, *J. Phys. Chem. B* 105 (2001) 4285–4292.
- [26] K. Sayama, H. Arakawa, *J. Photochem. Photobiol. A* 77 (1994) 243–247.
- [27] T. Hisatomi, M. Otani, K. Nakajima, K. Teramura, Y. Kako, D. Lu, T. Takata, Junko N. Kondo, K. Domen, *Chem. Mater.* 22 (2010) 3854–3861.
- [28] N. Bao, L. Shen, T. Takata, K. Domen, *Chem. Mater.* 20 (2008) 110–117.
- [29] L. Shen, N. Bao, P.E. Prevelige, A. Gupta, *J. Phys. Chem. C* 114 (2010) 2551–2559.
- [30] J. Zhang, Q. Xu, Z. Feng, M. Li, C. Li, *Angew. Chem. Int. Ed.* 47 (2008) 1766–1769.
- [31] Y. Misaki, H. Kato, A. Kudo, *Energy Environ. Sci.* 2 (2009) 306–314.
- [32] H. Husin, W. Su, H. Chen, C. Pan, S. Chang, J. Rick, W. Chuang, H. Sheu, B. Hwang, *Green Chem.* 13 (2011) 1745–1754.
- [33] S.W. Seo, S. Park, H.Y. Jeong, S.H. Kim, U. Sim, C.W. Lee, K.T. Nam, S.K. Hong, *Chem. Commun.* 48 (2012) 10452–10454.
- [34] H. Kato, H. Kobayashi, A. Kudo, *J. Phys. Chem. B* 106 (2002) 12441–12447.
- [35] W.J. Chun, A. Ishikawa, H. Fujisawa, T. Takata, J.N. Kondo, M. Hara, M. Kawai, Y. Matsumoto, K. Domen, *J. Phys. Chem. B* 107 (2003) 1798–1803.
- [36] S. Rtimi, R. Sanjines, C. Pulgarin, A. Houas, J.C. Lavanchy, J. Kiwi, J. Hazard. Mater. 260 (2013) 860–868.

- [37] Z. Wang, C.Y. Yang, T.Q. Lin, H. Yin, P. Chen, D.Y. Wan, F.F. Xu, F.Q. Huang, J.H. Lin, X.M. Xie, M.H. Jiang, *Adv. Funct. Mater.* 23 (2013) 5444–5450.
- [38] N. Zhang, M.Q. Yang, Z.R. Tang, Y.J. Xu, *ACS Nano* 8 (2014) 623–633.
- [39] Y.T. Liang, B.K. Vijayan, O.K. Lyandres, A. Gray, M.C. Hersam, *J. Phys. Chem. Lett.* 3 (2012) 1760–1765.
- [40] A.J. Huang, G. Natu, Z.Q. Ji, P. Hasin, Y.Y. Wu, *J. Phys. Chem. C* 115 (2011) 25109–25114.
- [41] J. Højberg, B.D. McCloskey, J. Hjelm, T. Vegge, K. Johansen, P. Norby, A.C. Luntz, *ACS Appl. Mater. Interfaces* 7 (2015) 4039–4047.
- [42] H.L. Guo, X.F. Wang, Q.Y. Qian, F.B. Wang, X.H. Xia, *ACS Nano* 3 (2009) 2653–2659.
- [43] Z. Zhang, Y. Yu, P. Wang, *ACS Appl. Mater. Interfaces* 4 (2012) 990–996.